

Mechanism of resonant x-ray magnetic scattering in NiO

Jun-ichi Igarashi and Manabu Takahashi

Faculty of Engineering, Gunma University, Kiryu, Gunma 376-8515, Japan
()

We study the resonant x-ray magnetic scattering (RXMS) around the K edge of Ni in the anti-ferromagnet NiO, by treating the $4p$ states of Ni as a band and the $3d$ states as localized states. We propose a mechanism that the $4p$ states are coupled to the magnetic order through the intra-atomic Coulomb interaction between the $4p$ and the $3d$ states and through the p - d mixing to the $3d$ states of neighboring Ni atoms. These couplings induce the orbital moment in the $4p$ band, and thereby give rise to the RXMS intensity at the K edge in the dipolar process. It is found that the spin-orbit interaction in the $4p$ band has negligibly small contribution to the RXMS intensity. The present model reproduces well the experimental spectra. We also discuss the azimuthal angle dependence of the intensity.

78.70.Ck, 71.20.Be, 75.50.Ee

I. INTRODUCTION

Resonant x-ray scattering has recently attracted much interest as a useful tool to investigate magnetic and orbital orders. The resonant enhancement for magnetic Bragg reflections has been observed in transition-metal compounds^{1,2,3,4} using synchrotron radiation with photon energy around the K edge. Also the resonant enhancement for the prohibited Bragg reflection corresponding to the orbital order has been observed in LaMnO_3 .⁵ The resonant scattering is described by a second order process that a photon is virtually absorbed by exciting a core electron to unoccupied states and then emitted by recombining the excited electron with the core hole. Therefore, for the K edge, the $4p$ states are involved in the dipolar process, while the $3d$ states are involved in the quadrupolar process. Since the $4p$ states are highly extended in space, they are rather sensitive to electronic structure at neighboring sites. This character is now well recognized in the resonant scattering for the orbital order in LaMnO_3 ; at the beginning, proposed was a mechanism that the intensity comes from the $4p$ states modified by the intra-atomic Coulomb interaction with the $3d$ electrons constituting the orbital order,⁶ but the subsequent studies of treating the $4p$ states as a band^{7,8,9,10} have revealed that the $4p$ states of Mn is mainly modified by the Jahn-Teller distortion via the oxygen potential on the neighboring sites, not by the intra-atomic Coulomb interaction.

In this paper, we study the mechanism of the resonant x-ray scattering for the magnetic order (RXMS) in NiO. We analyze the recent experiment of Neubeck *et al.*,⁴ paying special attentions to the band effects of the $4p$ states. In NiO, Ni atoms form an fcc lattice. It is a type II antiferromagnet (AF) with the Néel temperature $T_N = 523$ K. The order parameter is characterized by a wavevector \mathbf{Q} , which is directed to one of four body-diagonals in the fcc lattice. Therefore there exist four domains (K domains). The spin vector lies in the plane perpendicular to the AF modulation direction so that there are three possible directions (S domains). For example, the spins are directed to $(-1, -1, 2)$, $(2, -1, -1)$, or $(-1, 2, -1)$ in the K domain of $\mathbf{Q} = (\frac{1}{2}, \frac{1}{2}, \frac{1}{2})$. In total, we have 12 domains. In the RXMS experiment for NiO, the K domain is specified, but the S domains are mixed.⁴

For generating the RXMS intensity, orbitals have to couple to the magnetic order; in the dipolar process, the $4p$ states have to couple to the $3d$ states. Since such couplings are usually much smaller than those to the Jahn-Teller distortion in LaMnO_3 , the mechanism is much subtler than that for the orbital order in LaMnO_3 . The spin polarization alone in the $4p$ band cannot give rise to the RXMS intensity; if the amplitudes of exciting electron are summed for up and down spins, the total becomes the same at each site in the absence of the orbital moment. This leads to the cancellation of the amplitudes between different magnetic sublattices. The spin-orbit interaction in the $4p$ band may break this cancellation,^{3,4} but its effect will be shown to be negligibly small.

As discussed in our previous paper for CoO,¹¹ we propose that two couplings are effective to make the $4p$ states couple to the magnetic order: the intra-atomic Coulomb interaction between the $4p$ and $3d$ states, and the mixing of the $4p$ states with the $3d$ states of neighboring Ni atoms. To substantiate this observation, we use a tight-binding model for the $4p$ states, treating the $3d$ states within a cluster model. We will show that these couplings actually give rise to the RXMS spectra in agreement with the recent experiment.⁴ A caution is to be made on the intra-atomic Coulomb effect; without treating the $4p$ states as a band, the Coulomb interaction gives rise to too large RXMS intensities. Thus the $4p$ band effect has a role of reducing the effect of the Coulomb interaction. We have also a clear peak in the pre- K -edge region, which will be shown to come from the quadrupolar process. Since the $3d$ states strongly couple to the magnetic order, having this peak is not surprising. The present cluster model analysis, a slight extension of an atomic model analysis,⁴ reproduces well the experimental spectra.

This paper is organized as follows. In Sec. II, the present model is described, and the electronic structure is calculated on the basis of this model. In Sec. III, the formulation of the RXMS spectra is developed, and the calculated results are discussed in comparison with experiments. Section V is devoted to concluding remarks. In the Appendix, the geometrical factors are given in explicit forms.

II. 3D STATES

For describing the $3d$ states mixing to the $2p$ states of neighboring O sites, we start by the following model Hamiltonian:

$$\begin{aligned}
 H_0 = & \sum_{im\sigma} E_d(m) d_{im\sigma}^\dagger d_{im\sigma} + H_{3d-3d}^I \\
 & + \zeta_{3d} \sum_i \sum_{mm'\sigma\sigma'} \langle m\sigma | \ell \cdot \mathbf{s} | m'\sigma' \rangle d_{im\sigma}^\dagger d_{im'\sigma'} \\
 & + \sum_{j\ell\sigma} E_{2p} p_{j\ell\sigma}^\dagger p_{j\ell\sigma} + \sum_{\langle i,j \rangle} \sum_{\sigma\ell m} (t_{im,j\ell}^{2p,3d} p_{j\ell\sigma}^d \text{agger} d_{im\sigma} + H.c.).
 \end{aligned} \tag{2.1}$$

Operators $d_{im\sigma}$ and $p_{j\ell\sigma}$ represent the annihilation of an electron with spin σ in the $3d$ state m of the Ni site i and of an electron with spin σ in the $2p$ state ℓ of the O site j , respectively. The first term describes the energy of the $3d$ level. We take account of a point charge crystal-field splitting ($10Dq$) such that $E_d(e_g) = E_d + 6Dq$, $E_d(t_{2g}) = E_d - 4Dq$. The second term, H_{3d-3d}^I , represents the intra-atomic Coulomb interaction between the $3d$ states on Ni sites. Although the explicit form is omitted here, the matrix elements are written in terms of the Slater integrals $F^0(3d, 3d)$, $F^2(3d, 3d)$, and $F^4(3d, 3d)$. The third term represents the spin-orbit interaction of the $3d$ states. The fourth term represents the energy of the $2p$ level of O. The relative energy is given by the charge-transfer energy Δ defined by $\Delta = E_d - E_{2p} + nU$ for the d^n configuration with $U = F^0(3d, 3d) - \frac{2}{63}F^2(3d, 3d) - \frac{2}{63}F^4(3d, 3d)$. The last term represents the mixing of the Ni $3d$ states with the O $2p$ states. The mixing parameters $t_{im,j\ell}^{2p,3d}$ are defined by the Slater-Koster integrals, $(pd\sigma)_{2p,3d}$, $(pd\pi)_{2p,3d}$.¹² Most parameter values are assumed to be consistent with a previous cluster-model analysis¹³ and our previous electron correlation calculation.¹⁴ They are listed in Table I. We evaluate the atomic values within the Hartree-Fock (HF) approximation.¹⁵ For $F^0(3d, 3d)$, we use a rather smaller value than the atomic one by considering screening effects in solids, while for $F^2(3d, 3d)$ and $F^4(3d, 3d)$ we use the atomic values with multiplying a factor 0.8.

The ground state is calculated within this Hamiltonian as follows. We assume that each cluster consisting of a Ni atom and surrounding six O atoms is subjected to a molecular field coming from neighboring clusters; the exchange energy in the mean-field approximation is given by $H_{\text{ex}} = J(\mathbf{Q})\langle \mathbf{S} \rangle \cdot \mathbf{S}$, where \mathbf{S} represent the spin operator for the $3d$ states, and $J(\mathbf{Q})$ is the Fourier transform of the exchange constant with the AF modulation vector \mathbf{Q} . Since the Néel temperature T_N is given by $T_N = |J(\mathbf{Q})|S(S+1)/(3k_B)$ in the mean field approximation, the exchange energy is expressed as

$$H_{\text{ex}} = \frac{3|\langle \mathbf{S} \rangle|}{2S(S+1)} k_B T_N S \eta, \quad (2.2)$$

with the η axis pointing to one of the directions $(-1, -1, 2)$, $(2, -1, 1)$, or $(-1, 2, -1)$. We put $S = 1$, $|\langle \mathbf{S} \rangle| = 1$ for Ni atoms, and use the experimental value for T_N . Then we make numerical calculations, assuming that the ground state is given by a linear combination of the $3d^8$ configurations (45 states) and $3d^9\bar{\mathbf{L}}$ configuration (360 states) in each cluster, where $\bar{\mathbf{L}}$ indicates a state that a hole is in the $2p$ states of neighboring O sites. Diagonalizing the Hamiltonian matrix (405×405 dimensions), we obtain the ground state that the weight of being in the $3d^8$ configuration is 0.865 with the orbital moment $\langle L_z \rangle = 0.316$. This value is consistent with the value $\langle L_z \rangle = 0.32$ in the recent polarization analysis of nonresonant magnetic-scattering¹⁶ and in the LDA+ U calculation.¹⁷ Note that the calculated value of the orbital moment is sensitive to the assumed value of $10Dq$.

In the quadrupolar process of the RXMS, an electron is excited from the $1s$ state to the $3d$ states in the intermediate states. Such excited states are numerically calculated in a similar way to that for the ground state. We diagonalize the Hamiltonian matrix within the space of the $1s^1 3d^9$ configuration (10 states) and the $1s^1 3d^{10}\bar{\mathbf{L}}$ configuration (36 states), assuming that an attractive interaction $V_{3d}^c \sim 4$ eV works between the $3d$ electron and the core hole only in the core hole site. The energy of the core-hole is adjusted such that a peak in the pre-K-edge region is located at $\hbar\omega = 8330$ eV in the RXMS spectra (see Sec. IV).

III. 4P STATES

The RXMS involves a virtual process of a transition from the $1s$ state to the $4p$ states at Ni sites in the dipolar process, so that the $4p$ states are to be studied in detail. This section is devoted to the study of the $4p$ states in connection with the K -edge absorption spectra.

We use a tight-binding model for the $4p$ states. Although many other states such as $4s$ state at Ni sites and $3s$ state at O sites are mixed in such a rather-high-energy region, this model makes sense as an effective model for simply taking account of the $4p$ band effects; the $4p$ states keep their atomic character inside the atomic sphere even in solids. As relevant couplings to the magnetic order, we introduce the intra-atomic Coulomb interaction between the $4p$ and the $3d$ states, and the mixing of the $4p$ states with the $3d$ states in neighboring Ni atoms. Thereby a part of the Hamiltonian concerning the $4p$ states is given by

$$\begin{aligned} H_1 = & \sum_{in\sigma} E_{4p} a_{in\sigma}^\dagger a_{in\sigma} + \sum_{\langle i,i' \rangle} \sum_{\sigma n n'} \left(t_{in,i'n'}^{4p,4p} a_{in\sigma}^\dagger a_{i'n'\sigma} + \text{H.c.} \right) \\ & + \zeta_{4p} \sum_i \sum_{nn'\sigma\sigma'} \langle n\sigma | \ell \cdot \mathbf{s} | n'\sigma' \rangle a_{in\sigma}^\dagger a_{in'\sigma'} \\ & + H_{4p-3d}^I + \sum_{\sigma n m} \left(t_{in,i'm}^{4p,3d} a_{in\sigma}^\dagger d_{i'm\sigma} + \text{H.c.} \right), \end{aligned} \quad (3.1)$$

where $a_{in\sigma}$ represents the annihilation of an electron with spin σ in the $4p$ state n on Ni site i . The first and the second terms describe the $4p$ bands. The transfer integral $t_{in,i'n'}^{4p,4p}$ is written in terms of the Slater-Koster parameters, $(pp\sigma)_{4p,4p}$ and $(pp\pi)_{4p,4p}$.¹² We have the $4p$ band width ~ 20 eV, assuming $(pp\pi)_{4p,4p} \sim 3.5$ eV for the nearest-neighbor Ni-Ni distance, and the half of this value for the next-nearest-neighbor distance, with an empirical relation $(pp\pi)_{4p,4p} \sim -(pp\sigma)_{4p,4p}/4$. The value of E_{4p} is adjusted such that the peak in the K -edge absorption is located at $\hbar\omega = 8437$ eV. The third term represents the spin-orbit interaction in the $4p$ states. The HF atomic value is used for ζ_{4p} . The fourth term H_{4p-3d}^I represents the intra-atomic Coulomb interaction between the $4p$ states and the $3d$ states. The matrix elements are written in terms of the Slater integrals, $F^0(4p, 3d)$, $F^2(4p, 3d)$, $G^1(4p, 3d)$, and $G^3(4p, 3d)$. By the same reason as in H_{3d-3d}^I , the HF atomic values are used for $F^2(4p, 3d)$, $G^1(4p, 3d)$, and $G^3(4p, 3d)$ with multiplying a factor 0.8. The value of $F^0(4p, 3d)$ is rather ambiguous, since it can be absorbed into the value of E_{4p} . The last term describes the mixing of the $4p$ states with the $3d$ states of neighboring sites. The mixing parameter $t_{in,i'm}^{4p,3d}$ is written in terms of the Slater-Koster parameters, $(pd\sigma)_{4p,3d}$ and $(pd\pi)_{4p,3d}$. We assume $(pd\sigma)_{4p,3d} \sim -1.0$ eV together with an empirical relation $(pd\pi)_{4p,3d} \sim -(pd\sigma)_{4p,3d}/2$. Although this mixing is much smaller than the transfer between the $4p$ states, it is not neglected in the RXMS spectra, since it makes the $4p$ states couple to the magnetic order. The parameter values are listed in Table I.

We numerically calculate the $4p$ band as follows. The H_1 together with H_0 is represented in each Ni site within the space of states that one electron is in the $4p$ states with the $3d$ electrons in the ground state (6 states) and that a $3d$ electron is added to become the $3d^9$ -configuration (10 states). Such states in different Ni sites are coupled through the second and the last terms in Eq. (3.1), so that they form a band. Considering two Ni atoms in the unit cell due to the AF order, the Hamiltonian matrix has 32×32 dimensions for each wave vector, which is numerically diagonalized.

In the final state of the K -edge absorption and the intermediate states of RXMS, there is a hole in the $1s$ state, which attracts the $4p$ electron. Assuming that the core-hole potential works only within the core-hole site, we solve the potential problem with respect to a local Green's function defined by

$$\Pi_{0n\sigma;0n\sigma}(\omega) = -i \int_{-\infty}^{\infty} \langle T (b_{0\sigma}^\dagger(t) a_{0n\sigma}(t) a_{0n'\sigma'}^\dagger b_{0\sigma'}(0)) \rangle e^{i\omega t} dt, \quad (3.2)$$

where $b_{0\sigma}$ is the annihilation operator of the $1s$ state with spin σ at site 0, $\langle \dots \rangle$ the average over the ground state, and T the time ordering. Taking account of the multiple scattering due to the core-hole potential, we have

$$\Pi_{0n\sigma;0n\sigma}(\omega) = \sum_{n''\sigma''} \Pi_{0n\sigma;0n''\sigma''}^{(0)}(\omega) [I - V_{4p}^c \Pi^{(0)}(\omega)]_{0n''\sigma'';0n'\sigma'}^{-1}, \quad (3.3)$$

with

$$\Pi_{0n\sigma;0n\sigma}^{(0)}(\omega) = \sum_R \frac{\langle 0n\sigma | R \rangle \langle R | 0n'\sigma' \rangle}{\omega - (E_R + \epsilon_{\text{core}} - E_g) + i\Gamma/2}. \quad (3.4)$$

Here the state $|R\rangle$ represents the $4p$ band with energy E_R discussed above, and ϵ_{core} is the core hole energy. The life-time broadening width Γ and the core-hole potential V_{4p}^c are set to be 1.7 eV,⁴ and 3 eV, respectively.

The spectral function of the local Green's function, $I(\omega) = \sum_{n\sigma} (-1/\pi) \text{Im} \Pi_{0n\sigma;0n\sigma}(\omega)$, is proportional to the K -edge absorption spectra and the fluorescence spectra. Figure 2 shows $I(\omega)$ in comparison with the K edge fluorescence experiment.⁴ The solid and the broken lines represent the spectra for $V_{4p}^c = 0$ and 3 eV, respectively. The attractive interaction enhances the intensity in the low-energy side. It consists of two peaks. The peak in low-energy region corresponds to the K -edge peak in the experimental spectra. We are mainly interested in the energy region of this peak in the RXMS spectra. The peak in high energy region may correspond to the peak around $\hbar\omega = 8365$ eV in the experimental spectra, but the calculated peak is too large. This discrepancy may come from using the $4p$ tight-binding model; in reality, it is likely to become much broader through the mixing to other states such as the $4s$ state of Ni and $3s$ states of O.

IV. RESONANT X-RAY MAGNETIC SCATTERING

A. Procedure of calculation

The magnetic scattering amplitude has been reviewed by several authors.^{18,19,20} We summarize here the expression of the amplitude in a form suitable to the present calculation. The scattering geometry is shown in Fig. 3; photon

with frequency ω , momentum \mathbf{k}_i and polarization μ ($= \sigma$ or π) is scattered into the state with momentum \mathbf{k}_f and polarization μ' ($= \sigma'$ or π'). For the system with two magnetic sublattices A and B in the AF order, the cross section for elastic scattering at magnetic Bragg peaks is given by

$$\left. \frac{d\sigma}{d\Omega'} \right|_{\mu \rightarrow \mu'} \propto |T_{\mu \rightarrow \mu'}^A(\mathbf{G}, \omega) - T_{\mu \rightarrow \mu'}^B(\mathbf{G}, \omega)|^2, \quad (4.1)$$

with

$$\begin{aligned} T_{\mu \rightarrow \mu'}^\eta(\mathbf{G}, \omega) = & -\frac{i\hbar\omega}{mc^2} \left(\frac{1}{2} \mathbf{L}^\eta(\mathbf{G}) \cdot \mathbf{A}'' + \mathbf{S}^\eta(\mathbf{G}) \cdot \mathbf{B} \right) \\ & + J_{\mu \rightarrow \mu'}^\eta(\mathbf{G}, \omega) + L_{\mu \rightarrow \mu'}^\eta(\mathbf{G}, \omega). \end{aligned} \quad (4.2)$$

where $\mathbf{G} = \mathbf{k}_f - \mathbf{k}_i$ is the scattering vector.

The first term in eq. (4.2) represents a *non-resonant* term, where m and c are the electron mass and the velocity of photon, respectively.²⁰ \mathbf{A}'' and \mathbf{B} are given by

$$\mathbf{A}'' = \mathbf{A}' - (\mathbf{A}' \cdot \hat{\mathbf{G}})\hat{\mathbf{G}}, \quad \mathbf{A}' = -4 \sin^2 \theta (\hat{\epsilon}' \times \hat{\epsilon}), \quad (4.3)$$

$$\mathbf{B} = \hat{\epsilon}' \times \hat{\epsilon} + (\hat{\mathbf{k}}_f \times \hat{\epsilon}')(\hat{\mathbf{k}}_f \cdot \hat{\epsilon}) - (\hat{\mathbf{k}}_i \times \hat{\epsilon})(\hat{\mathbf{k}}_i \cdot \hat{\epsilon}') - (\hat{\mathbf{k}}_f \times \hat{\epsilon}') \times (\hat{\mathbf{k}}_i \times \hat{\epsilon}), \quad (4.4)$$

where $\hat{\epsilon}$ and $\hat{\epsilon}'$ are the initial and scattered polarizations, and $\hat{\mathbf{k}}_i$, $\hat{\mathbf{k}}_f$, and $\hat{\mathbf{G}}$ are normalized vectors of \mathbf{k}_i , \mathbf{k}_f , and \mathbf{G} . $\mathbf{L}^\eta(\mathbf{G})$ and $\mathbf{S}^\eta(\mathbf{G})$ stand for the Fourier transform of the orbital and spin angular momentum densities, which values are known from the recent non-resonant RXS experiment:^{4,16} $|\mathbf{L}(\mathbf{G})|(|\mathbf{S}(\mathbf{G})|) = 0.26$ (0.82), 0.24 (0.60), and 0.12 (0.20) for $\mathbf{G} = (\frac{1}{2}, \frac{1}{2}, \frac{1}{2})$, $(\frac{3}{2}, \frac{3}{2}, \frac{3}{2})$, and $(\frac{5}{2}, \frac{5}{2}, \frac{5}{2})$, respectively. We insert these experimental values into Eq. (4.2). The local moments of orbital and spin are give by $\mathbf{L}^\eta(\mathbf{G})$ and $\mathbf{S}^\eta(\mathbf{G})$ with $\mathbf{G} \rightarrow 0$. The above experimental values are consistent with the present ground-state calculation in Sec. II.

The second term in Eq. (4.2) represents the resonant contribution from the dipolar process. It is expressed by a second-order process that a photon is virtually absorbed by exciting the $1s$ electron to the $4p$ states and then emitted by recombining the excited electron with the $1s$ core hole. The corresponding amplitude is expressed as

$$J_{\mu \rightarrow \mu'}^\eta(\mathbf{G}, \omega) = \sum_{\alpha\alpha'} (P'^{\mu'})_\alpha M_{\alpha\alpha'}^\eta(\omega) P_{\alpha'}^\mu, \quad (4.5)$$

with the scattering tensor

$$M_{\alpha\alpha'}^\eta(\omega) = \sum_{\Lambda} \frac{m\omega_{\Lambda g}^2 \langle g|x_\alpha|\Lambda\rangle \langle \Lambda|x_{\alpha'}|g\rangle}{\hbar\omega - (E_\Lambda - E_g) + i\Gamma/2}. \quad (4.6)$$

The geometrical factors P^μ , $P'^{\mu'}$ are given in explicit forms in the Appendix. In Eq. (4.6), $\omega_{\Lambda g} = (E_\Lambda - E_g)/\hbar$, and x_α 's stand for the dipole operators, $x_1 = x$, $x_2 = y$, and $x_3 = z$ in the coordinate frame fixed to the crystal axes. The ground state $|g\rangle$ has an energy E_g . The intermediate state $|\Lambda\rangle$ consists of an excited electron on the $4p$ states and a hole on the $1s$ state with energy E_Λ . In the presence of the core-hole potential, it is convenient to rewrite the scattering tensor in terms of the local Green's function defined in Sec. III. We have

$$M_{\alpha\alpha'}^\eta(\omega) = A_p^2 m\omega_c^2 \sum_{\sigma} \Pi_{0\alpha\sigma, 0\alpha\sigma}(\omega), \quad (4.7)$$

where site 0 is to belong to sublattice η , and $\hbar\omega_c \approx 8350$ eV. The A_p is the dipole matrix element defined by $A_p = \langle 4p|r|1s\rangle = \int_0^\infty R_{4p}(r)rR_{1s}(r)r^2 dr$ with $R_{1s}(r)$ and $R_{4p}(r)$ being the radial wavefunctions for the $1s$ and $4p$ states. We evaluate it as $A_p = 1.52 \times 10^{-11}$ cm within the HF approximation¹⁵ in the $3d^8$ configuration of a free Ni ion. The amplitudes at A and B sublattices are nearly cancelled out, leading to an antisymmetric form for the difference:

$$M^A(\omega) - M^B(\omega) = \begin{pmatrix} 0 & a & c \\ -a & 0 & b \\ -c & -b & 0 \end{pmatrix}, \quad (4.8)$$

with a , b , and c being some complex numbers.

The third term in Eq. (4.2) represents the resonant contribution from the quadrupolar process. The corresponding amplitude is expressed as

$$L_{\mu \rightarrow \mu'}^{\eta}(\mathbf{G}, \omega) = \sum_{\gamma\gamma'} (Q^{\mu'})_{\gamma} N_{\gamma\gamma'}^{\eta}(\omega) Q_{\gamma'}^{\mu}, \quad (4.9)$$

with the scattering tensor,

$$N_{\gamma\gamma'}^{\eta}(\omega) = \frac{k^2}{12} \sum_{\Lambda'} \frac{m\omega_{\Lambda'g}^2 \langle g|z_{\gamma}|\Lambda'\rangle \langle \Lambda'|z_{\gamma'}|g\rangle}{\hbar\omega - (E_{\Lambda'} - E_g) + i\Gamma/2}. \quad (4.10)$$

The geometrical factors, Q^{μ} , $Q^{\mu'}$, are given in explicit forms in the Appendix. In Eq. (4.10), k is the wavevector of the incident (and scattered) photon, $\sim 4.2 \times 10^8 \text{ cm}^{-1}$, $\omega_{\Lambda'g} = (E_{\Lambda'} - E_g)/\hbar$, and z_{μ} 's stand for the quadrupole operators, $z_1 = (\sqrt{3}/2)(x^2 - y^2)$, $z_2 = (1/2)(3z^2 - r^2)$, $z_3 = \sqrt{3}yz$, $z_4 = \sqrt{3}zx$, and $z_5 = \sqrt{3}xy$ in the coordinate frame fixed to the crystal axes. The intermediate states $|\Lambda'\rangle$ consist of an excited electron on the $3d$ states and a hole on the $1s$ states with energy $E_{\Lambda'}$, which are evaluated by following the procedure described in Sec II. The scattering amplitude $N_{\gamma\gamma'}^{\eta}(\omega)$ contains the square of the quadrupole matrix element $A_d = \langle 3d|r^2|1s\rangle = \int_0^{\infty} R_{3d}(r)r^2R_{1s}(r)r^2dr$, with $R_{3d}(r)$ being the radial wavefunction of a free Ni ion. We evaluate it as $A_d = 2.10 \times 10^{-20} \text{ cm}^2$ within the HF approximation in the $3d^8$ configuration. Similar to the dipolar process, the scattering tensors $N^A(\omega)$ and $N^B(\omega)$ are nearly cancelled out, leading to an antisymmetric form for the difference:

$$N^A(\omega) - N^B(\omega) = \begin{pmatrix} 0 & d & e & f & g \\ -d & 0 & h & p & q \\ -e & -h & 0 & r & s \\ -f & -p & -r & 0 & t \\ -g & -q & -s & -t & 0 \end{pmatrix}, \quad (4.11)$$

with $\tilde{d} \sim t$ being some complex numbers. Note that this difference would vanish if the spin-orbit interaction in the $3d$ states were absent. This is consistent with the prediction by Loversey.²¹

B. Calculated results

In this subsection, we discuss the RXMS spectra in comparison with the recent experiment of Neubeck *et al.*⁴ In their experiment, the K domain of $\mathbf{Q} = (\frac{1}{2}, \frac{1}{2}, \frac{1}{2})$ is selected, but the contributions from different S domains are not separated. Fortunately the relative volumes for three S domains have been determined such that $0.55(S_1)$, $0.4(S_2)$, $0.05(S_3)$ for $\mathbf{Q} = (\frac{1}{2}, \frac{1}{2}, \frac{1}{2})$, $0.63(S_1)$, $0.37(S_2)$, $0(S_3)$ for $\mathbf{Q} = (\frac{3}{2}, \frac{3}{2}, \frac{3}{2})$, and $0.26(S_1)$, $0.33(S_2)$, $0.41(S_3)$ for $\mathbf{Q} = (\frac{5}{2}, \frac{5}{2}, \frac{5}{2})$. In the following, we average the spectra over three S domains multiplying the weights of these relative volumes.

Figure 4 shows the spectra thus calculated as a function of photon energy for $\mathbf{G} = (\frac{1}{2}, \frac{1}{2}, \frac{1}{2})$. The azimuthal angle ψ is set to be zero such that the scattering plane contains the $(1, -1, 0)$ crystal axis, corresponding to the experimental situation. The left panels show the spectra for the $\sigma \rightarrow \sigma'$ channel. Only one peak is found at $\hbar\omega = 8330 \text{ eV}$ in the pre- K -edge region, in agreement with the experiment. Since the dipolar process is forbidden in this polarization, this peak arises from the quadrupolar process. A strong anti-resonant dip is seen in the low energy side of the peak, which comes from an interference of the non-resonant process with the quadrupolar process. The experimental intensity in the high energy side of the peak is much smaller than the calculated intensity. This discrepancy may be related to the lack of absorption correction on the experimental spectra, which correction should make the intensity in the high energy side the same as that in the low energy side. This observation conversely suggests the size of the absorption correction. The right panels show the spectra for the $\sigma \rightarrow \pi'$ channel. Similar to the $\sigma \rightarrow \sigma'$ channel, we find a sharp peak at $\hbar\omega = 8330 \text{ eV}$, which arises from the quadrupolar process. The intensity for the energy far below $\hbar\omega = 8330 \text{ eV}$ is much smaller than the value for the $\sigma \rightarrow \sigma'$ channel. In addition, we have several structures in the high-energy side of the peak. As plotted by the long-dashed line, the non-resonant process and the quadrupolar process cannot give rise to sufficient intensities, indicating that the intensity mainly comes from the dipolar process. We have checked the effect of the spin-orbit interaction in the $4p$ band by calculating the spectra with neglecting that interaction; no visible change is found. We have a peak around $\hbar\omega = 8346 \text{ eV}$, in agreement with the experiment. To this peak, the intra-atomic Coulomb interaction between the $4p$ and the $3d$ states contributes substantially (compare the solid line with the dashed one). The experimental intensity, which is smaller than the calculated one, should be enhanced by absorption correction. We should emphasize here that the dipolar contribution becomes more than 10 times as

large as the present values, too large in comparison with the experimental one, if the transfer of the $4p$ electron to neighboring sites is neglected.²² Therefore, the $4p$ band effect is very important for reproducing the experimental spectra. A large peak at $\hbar\omega \sim 8365$ eV is regarded as an artifact of using the tight-binding model, as mentioned in Sec. III.

Figure 5 shows the spectra as a function of photon energy, at $\psi = 0$ for $\mathbf{G} = (\frac{3}{2}, \frac{3}{2}, \frac{3}{2})$. The left panels show the spectra for the $\sigma \rightarrow \sigma'$ channel. The spectral shape is quite similar to that for $\mathbf{G} = (\frac{1}{2}, \frac{1}{2}, \frac{1}{2})$. The right panels show the spectra for the $\sigma \rightarrow \pi'$ channel. The non-resonant intensity is larger than that for $\mathbf{G} = (\frac{1}{2}, \frac{1}{2}, \frac{1}{2})$. We find a sharp peak at $\hbar\omega = 8330$ eV, which arises from the quadrupolar process. In the high-energy side of this peak, we also have several structures arising from the dipolar process; a peak around $\hbar\omega = 8346$ eV agrees well with the experiment.

Figure 6 shows the spectra as a function of photon energy for $\mathbf{G} = (\frac{5}{2}, \frac{5}{2}, \frac{5}{2})$. The azimuthal angle ψ is now set to be 270° , corresponding to the experimental situation. The right panels show the spectra for the $\sigma \rightarrow \pi'$ channel. For the peak at $\hbar\omega \sim 8330$ eV, an anti-resonant dip now moved to the high-energy side. We also find a broad peak around $\hbar\omega \sim 8340$ eV, owing to the dipolar process.

Figure 7 shows the spectra as a function of the azimuthal angle ψ for $\mathbf{G} = (\frac{1}{2}, \frac{1}{2}, \frac{1}{2})$, in comparison with the experiment. The lowest panel shows the intensity of the peak at $\hbar\omega = 8346$ eV in the main- K -edge region for the $\sigma \rightarrow \pi'$ channel. We multiply a factor such that the calculated values at $\psi = 0$ becomes close to the experimental one. The variation resembles to a dependence of $\sin^2 \psi$, consistent with the dominant contribution of the dipolar process. The top and middle panels show the intensities of the peaks at $\hbar\omega = 8330$ eV in the pre- K -edge region for $\sigma \rightarrow \sigma'$ and the $\sigma \rightarrow \pi'$ channels, respectively. We multiply a same factor in both cases such that the values at $\psi = 0$ become close to the experimental ones. The variation in the top panel looks simply a 90° -shift of the curve in the lowest panel. This is a little surprising, since we expect a more complex shape from the quadrupolar process. The curve in the middle panel has an extra peak. This may be related to the fact that the dipolar contribution remains in this peak. Such an extra peak is not clear in the experiment.

V. CONCLUDING REMARKS

We have studied the RXMS around the K edge in the antiferromagnet NiO, treating the $4p$ states as a band and the $3d$ states as localized states. We have proposed a mechanism that the $4p$ states are coupled to the magnetic order through the intra-atomic Coulomb interaction between the $4p$ and $3d$ states, and through the p - d mixing to the $3d$ states of neighboring Ni atoms. Thereby the orbital moment is induced in the $4p$ states, giving rise to the RXMS intensity in the dipolar process. The calculated spectra in the present model have reproduced well the experimental ones.⁴ Different from previous analyses,^{3,4} the effect of the spin-orbit interaction in the $4p$ band is found negligibly small within the present model. This reminds us of the magnetic circular dichroism (MCD) for the K -edge absorption in the ferromagnetic metals Fe, Co, and Ni.²³ It is known that the MCD intensity is mainly generated by the orbital moment induced in the $4p$ band through the mixing to the $3d$ states of neighboring atoms, not through the spin-orbit interaction in the $4p$ band.²⁴

We have also obtained a peak in the pre- K -edge region, in agreement with a previous analysis in the atomic model.⁴ This arises from the quadrupole process, showing a contrast to the pre- K -edge peak in the resonant scattering for the orbital order in LaMnO₃. The latter is predicted to be generated by the dipolar process,¹⁰ where the states of p symmetry (seen from the Mn atoms) have weights in the pre- K -edge region by mixing to the $3d$ states of neighboring Mn atoms. Usually the intensity of the quadrupolar process is much smaller than that of the dipolar process, but the dipolar contribution cannot become large in the present case because of a weak coupling of the $4p$ states to the magnetic order.

Furthermore, we have discussed the azimuthal-angle dependence of the spectra. The curve for the pre- K -edge peak, which comes from the quadrupolar process, looks simply a 90° -shift of the curve for the main- K -edge peak, which comes mainly from the dipolar process.

Finally, we would like to stress again that the tight-binding model is a first approach for taking account of the $4p$ band effects. More realistic band calculations are desirable for obtaining more quantitative results.

ACKNOWLEDGMENTS

We would like to thank W. Neubeck for kindly informing the experimental data for NiO prior to publication. This work was partially supported by a Grant-in-Aid for Scientific Research from the Ministry of Education, Science, Sports and Culture, Japan.

APPENDIX A: GEOMETRICAL FACTOR

We summarize here the expressions of geometrical factors for the dipolar and quadrupolar processes. The detailed derivation is given in Ref. [11]. For the scattering vectors $\mathbf{G} = (\frac{1}{2}, \frac{1}{2}, \frac{1}{2})$, $(\frac{3}{2}, \frac{3}{2}, \frac{3}{2})$, and $(\frac{5}{2}, \frac{5}{2}, \frac{5}{2})$, the geometrical factor P^μ ($\mu = \sigma$ or π) for incident photon in the dipolar process is given by

$$\begin{aligned} (P^\sigma)_1 &= (\cos \beta \cos \psi + \sin \psi) / \sqrt{2}, \\ (P^\sigma)_2 &= (\cos \beta \cos \psi - \sin \psi) / \sqrt{2}, \\ (P^\sigma)_3 &= -\sin \beta \cos \psi, \end{aligned} \tag{A1}$$

$$\begin{aligned} (P^\pi)_1 &= [\sin \theta (\cos \beta \sin \psi - \cos \psi) + \cos \theta \sin \beta] / \sqrt{2}, \\ (P^\pi)_2 &= [\sin \theta (\cos \beta \sin \psi + \cos \psi) + \cos \theta \sin \beta] / \sqrt{2}, \\ (P^\pi)_3 &= (-\sin \theta \sin \beta \sin \psi + \cos \theta \cos \beta), \end{aligned} \tag{A2}$$

where with $\beta = \arccos \sqrt{1/3}$, and θ represents the Bragg angle. The azimuthal angle $\psi = 0$ corresponds to the scattering plane containing the $(1, -1, 0)$ crystal axis. The geometrical factor $P'^{\mu'}$ ($\mu' = \sigma'$ or π') for the scattered photon is given by replacing $\sin \theta$ by $-\sin \theta$ in Eqs. (A1) and (A2).

Also, the geometrical factor Q^μ ($\mu = \sigma$ or π) for incident photon in the quadrupolar process is given by

$$\begin{aligned} (Q^\sigma)_1 &= -\cos \theta \cos \beta \cos 2\psi - \sin \theta \sin \beta \sin \psi, \\ (Q^\sigma)_2 &= (\sqrt{3}/2) \cos \theta \sin^2 \beta \sin 2\psi + (\sqrt{3}/2) \sin \theta \sin 2\beta \cos \psi, \\ (Q^\sigma)_3 &= -\cos \theta \sin \beta (\cos \beta \sin 2\psi + \cos 2\psi) / \sqrt{2} \\ &\quad - \sin \theta (\cos 2\beta \cos \psi - \cos \beta \sin \psi) / \sqrt{2}, \\ (Q^\sigma)_4 &= -\cos \theta \sin \beta (\cos \beta \sin 2\psi - \cos 2\psi) / \sqrt{2} \\ &\quad - \sin \theta (\cos 2\beta \cos \psi + \cos \beta \sin \psi) / \sqrt{2}, \\ (Q^\sigma)_5 &= \cos \theta [1 - (1/2) \sin^2 \beta] \sin 2\psi - (1/2) \sin \theta \sin 2\beta \cos \psi, \\ (Q^\pi)_1 &= -(1/2) \sin 2\theta \cos \beta \sin 2\psi - \cos 2\theta \sin \beta \cos \psi, \\ (Q^\pi)_2 &= -(\sqrt{3}/4) \sin 2\theta \sin^2 \beta \cos 2\psi - (\sqrt{3}/2) \cos 2\theta \sin 2\beta \sin \psi \\ &\quad - (\sqrt{3}/2) \sin 2\theta [1 - (3/2) \sin^2 \beta], \\ (Q^\pi)_3 &= (1/2\sqrt{2}) \sin 2\theta \sin \beta (\cos \beta \cos 2\psi - \sin 2\psi) \\ &\quad + \cos 2\theta (\cos 2\beta \sin \psi + \cos \beta \cos \psi) / \sqrt{2} \\ &\quad - (3/4\sqrt{2}) \sin 2\theta \sin 2\beta, \\ (Q^\pi)_4 &= (1/2\sqrt{2}) \sin 2\theta \sin \beta (\cos \beta \cos 2\psi + \sin 2\psi) \\ &\quad + \cos 2\theta (\cos 2\beta \sin \psi - \cos \beta \cos \psi) / \sqrt{2} \\ &\quad - (3/4\sqrt{2}) \sin 2\theta \sin 2\beta, \\ (Q^\pi)_5 &= -(1/2) \sin 2\theta [1 - (1/2) \sin^2 \beta] \cos 2\psi \\ &\quad + (1/2) \cos 2\theta \sin 2\beta \sin \psi - (3/4) \sin 2\theta \sin^2 \beta. \end{aligned} \tag{A3}$$

The geometrical factor $Q'^{\mu'}$ ($\mu' = \sigma'$ or π') for scattered photon is given by replacing $\sin \theta$ and $\sin 2\theta$ by $-\sin \theta$ and $-\sin 2\theta$, respectively, in Eqs. (A3) and (A4).

¹ J. P. Hill, C.-C. Kao and D. F. McMorrow, Phys. Rev. B **55**, R8662 (1997).

² W. Neubeck, C. Vettier, K.-B. Lee and F. de Bergevin, Phys. Rev. B **60**, R9912 (1999).

³ A. Stunault, F. de Bergevin, D. Wermeille, C. Vettier, Th. Brückel, N. Bernhoeft, G. J. McIntyre, and J. Y. Henry, Phys. Rev. B **60**, 10170 (1999).

- ⁴ W. Neubeck, C. Vettier, F. de Bergevin, F. Yakhou, D. Mannix, O. Bengone, M. Alouani, and A. Barbier, preprint.
- ⁵ Y. Murakami, J. P. Hill, D. Gibbs, M. Blume, I. Koyama, M. Tanaka, H. Kawata, T. Arima, Y. Tokura, K. Hirota and Y. Endoh, Phys. Rev. Lett. **81**, 582 (1998).
- ⁶ S. Ishihara and S. Maekawa, Phys. Rev. Lett. **80**, 3799 (1998); Phys. Rev. **B 58**, 13449 (1998).
- ⁷ I. S. Elfimov, V. I. Anisimov and G. Sawatzky, Phys. Rev. Lett. **82**, 4264 (1999).
- ⁸ M. Benfatto, Y. Joly and C. R. Natori, Phys. Rev. Lett. **83**, 636 (1999).
- ⁹ M. Takahashi, J. Igarashi and P. Fulde, J. Phys. Soc. Jpn. **68**, 2530 (1999).
- ¹⁰ M. Takahashi, J. Igarashi and P. Fulde, J. Phys. Soc. Jpn. **69**, 1614 (2000).
- ¹¹ J. Igarashi and M. Takahashi, J. Phys. Soc. Jpn. **69**, 4087 (2000).
- ¹² J. C. Slater and G. F. Koster, Phys. Rev. **94**, 1498 (1954).
- ¹³ J. van Elp, H. Eskes, P. Kuiper, and G. A. Sawatzky, Phys. Rev. **B 45**, 1612 (1992).
- ¹⁴ M. Takahashi and J. Igarashi, Phys. Rev. B **54**, 13566 (1996).
- ¹⁵ R. Cowan, *The Theory of Atomic Structure and Spectra* (University of California Press, Berkeley, 1981).
- ¹⁶ V. Fernandez, C. Vettier, F. de Bergevin, C. Giles, and W. Neubeck, Phys. Rev. B **57**, 7870 (1998).
- ¹⁷ S. K. Kwon and B. I. Min, Phys. Rev. B **62**, 73 (2000).
- ¹⁸ F. de Bergevin and M. Brunel, Acta Crystallogr., Sect. A: Cryst. Phys., Diffr., Theor. Gen. Crystallogr. **37**, 324 (1981).
- ¹⁹ M. Blume, J. Appl. Phys. **57**, 3615 (1985).
- ²⁰ M. Blume and D. Gibbs, Phys. Rev. B **37**, 1779 (1988).
- ²¹ S. W. Loversey, J. Phys. Condens. Matter **10**, 2505 (1998).
- ²² In the previous analysis of the RXMS spectra for CoO within a cluster model (Ref. [11]), we had to assume that the values of the intra-atomic Coulomb interaction is considerably smaller than the atomic values for obtaining the reasonable (not too large) RXMS intensities.
- ²³ G. Schütz, W. Wagner, W. Wilhelm, P. Kienle, R. Zeller, R. Frahn, and G. Materlik, Phys. Rev. Lett. **58**, 737 (1987).
- ²⁴ J. Igarashi and K. Hirai, Phys. Rev. B **50**, 17820 (1994); **53**, 6442 (1996).

TABLE I. Parameter values for the tight-binding model of NiO in units of eV.

Parameter ^a		Parameter ^b	
F_{dd}^0	6.5	F_{pd}^0	2.5
F_{dd}^2	9.8	F_{pd}^2	1.9
F_{dd}^4	6.1	G_{pd}^1	0.68
Δ	6.0	G_{pd}^3	0.59
$(pd\sigma)_{2p,3d}$	-1.4	$(pp\sigma)_{4p,4p}$	3.5
$(pd\pi)_{2p,3d}$	0.63	$(pp\pi)_{4p,4p}$	-0.88
$10Dq$	0.50	$(pd\sigma)_{4p,3d}$	-1.0
		$(pd\pi)_{4p,3d}$	0.50
ζ_{3d}	0.096 (0.12 ^c)	ζ_{4p}	0.098

^a Values in the $1s^23d^8$ configuration.

^b Values in the $1s^13d^84p^1$ configuration.

^c Value in the $1s^13d^9$ configuration.

FIG. 1. Finite section of a NiO crystal. Only Ni atoms are shown. Wave vector $\mathbf{Q} = (\frac{1}{2}, \frac{1}{2}, \frac{1}{2})$ characterizes an antiferromagnetic modulation direction. Three arrows in a plane perpendicular to \mathbf{Q} indicate possible spin directions (S domains). Spins for solid, grey, and open circles align alternately.

FIG. 2. Spectral function $I(\omega)$ for the local Green's function for the $4p$ states (lower panel), in comparison with the K -edge fluorescence spectra (upper panel).⁴ Solid and broken lines represent the spectra calculated with the core-hole potential $V_{4p}^c = 0$ and 3 eV, respectively.

FIG. 3. Scattering geometry of x ray scattering. Incident photon with wave vector \mathbf{k}_i and polarization σ or π is scattered into the state with wave vector \mathbf{k}_f and polarization σ' or π' at Bragg angle θ . The sample crystal is rotated by azimuthal angle ψ around the scattering vector $\mathbf{G} = \mathbf{k}_f - \mathbf{k}_i$.

FIG. 4. Magnetic scattering spectra for $\mathbf{G} = (\frac{1}{2}, \frac{1}{2}, \frac{1}{2})$ at $\psi = 0^\circ$, as a function of photon energy, in comparison with the experiment. The upper panels show the experimental spectra without absorption correction.⁴ The left and right panels show the intensity for the $\sigma \rightarrow \sigma'$ channel, and that for the $\sigma \rightarrow \pi'$ channel, respectively. In the right and lower panel, the dashed line represents the intensity by neglecting the intra-atomic Coulomb interaction between the $4p$ and the $3d$ states, and the long-dashed line represents the contribution from the non-resonant and the quadrupolar processes.

FIG. 5. Magnetic scattering spectra for $\mathbf{G} = (\frac{3}{2}, \frac{3}{2}, \frac{3}{2})$ at $\psi = 0^\circ$, as a function of photon energy, in comparison with the experiment. The upper panels show the experimental spectra without absorption correction.⁴ The left and right panels show the intensity for the $\sigma \rightarrow \sigma'$ channel and that for the $\sigma \rightarrow \pi'$ channel, respectively.

FIG. 6. Magnetic scattering spectra for $\mathbf{G} = (\frac{5}{2}, \frac{5}{2}, \frac{5}{2})$ at $\psi = 270^\circ$, as a function of photon energy, in comparison with the experiment. The upper panels show the experimental spectra without absorption correction.⁴ The left and right panels show the intensity for the $\sigma \rightarrow \sigma'$ channel and that for the $\sigma \rightarrow \pi'$ channel, respectively.

FIG. 7. Magnetic scattering intensity as a function of azimuthal angle ψ , for $\mathbf{G} = (\frac{1}{2}, \frac{1}{2}, \frac{1}{2})$, in comparison with the experiment. The open circles represent the experimental intensities.⁴ The top and middle panels are for the peak at $\hbar\omega = 8330$ eV in the pre- K -edge region for the $\sigma \rightarrow \sigma'$ and $\sigma \rightarrow \pi'$ channels, respectively. The lowest panel is for the peak at $\hbar\omega = 8346$ eV in the main- K -edge region for the $\sigma \rightarrow \pi'$ channel.

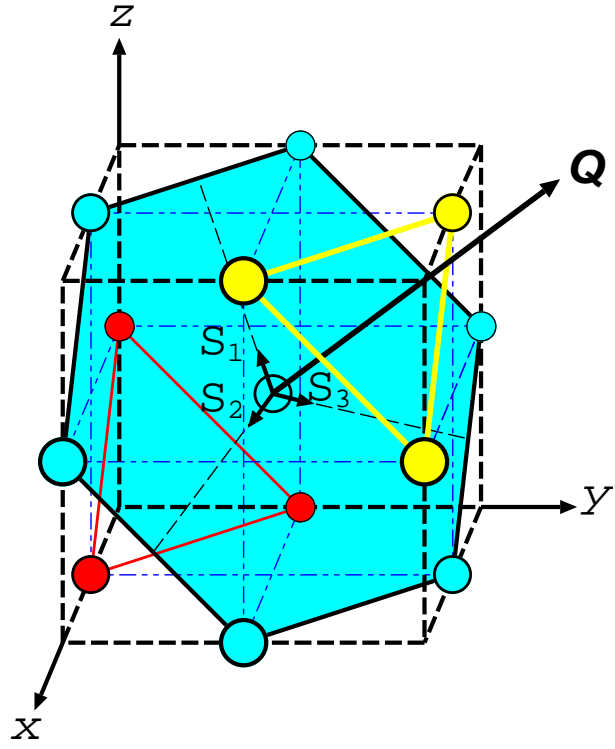


FIG. 1.

J. Igarashi and M. Takahashi

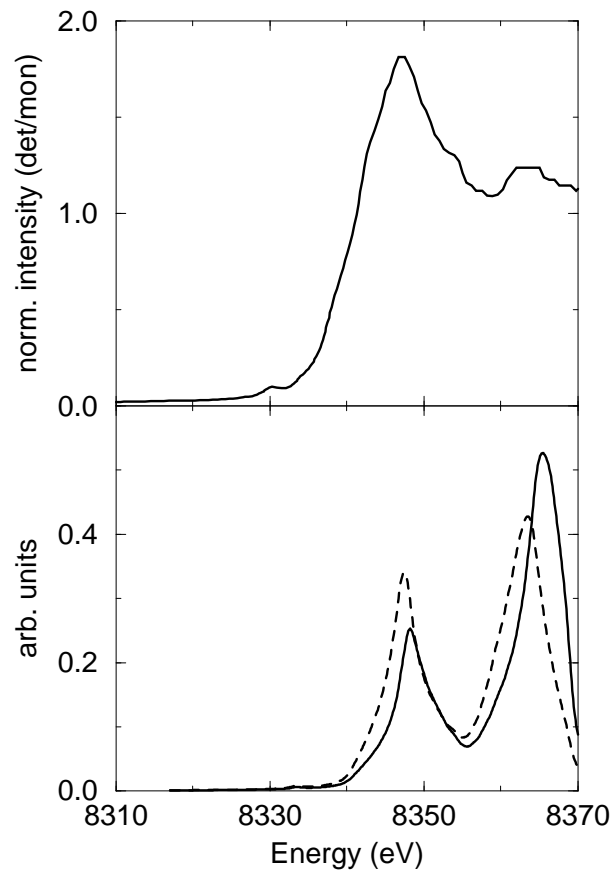


FIG. 2.

J. Igarashi and M. Takahashi

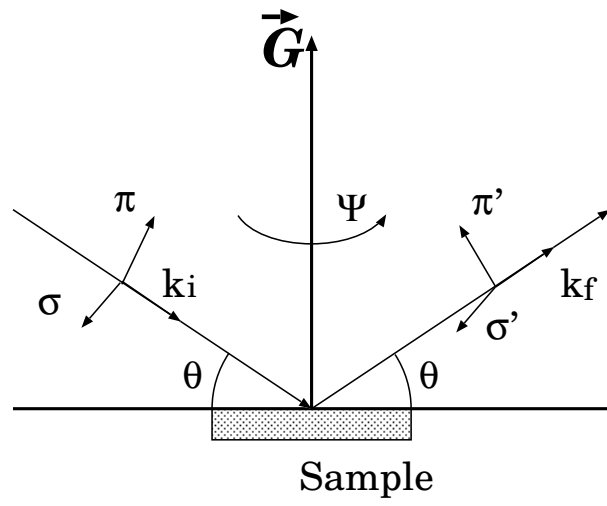


FIG. 3.

J. Igarashi and M. Takahashi

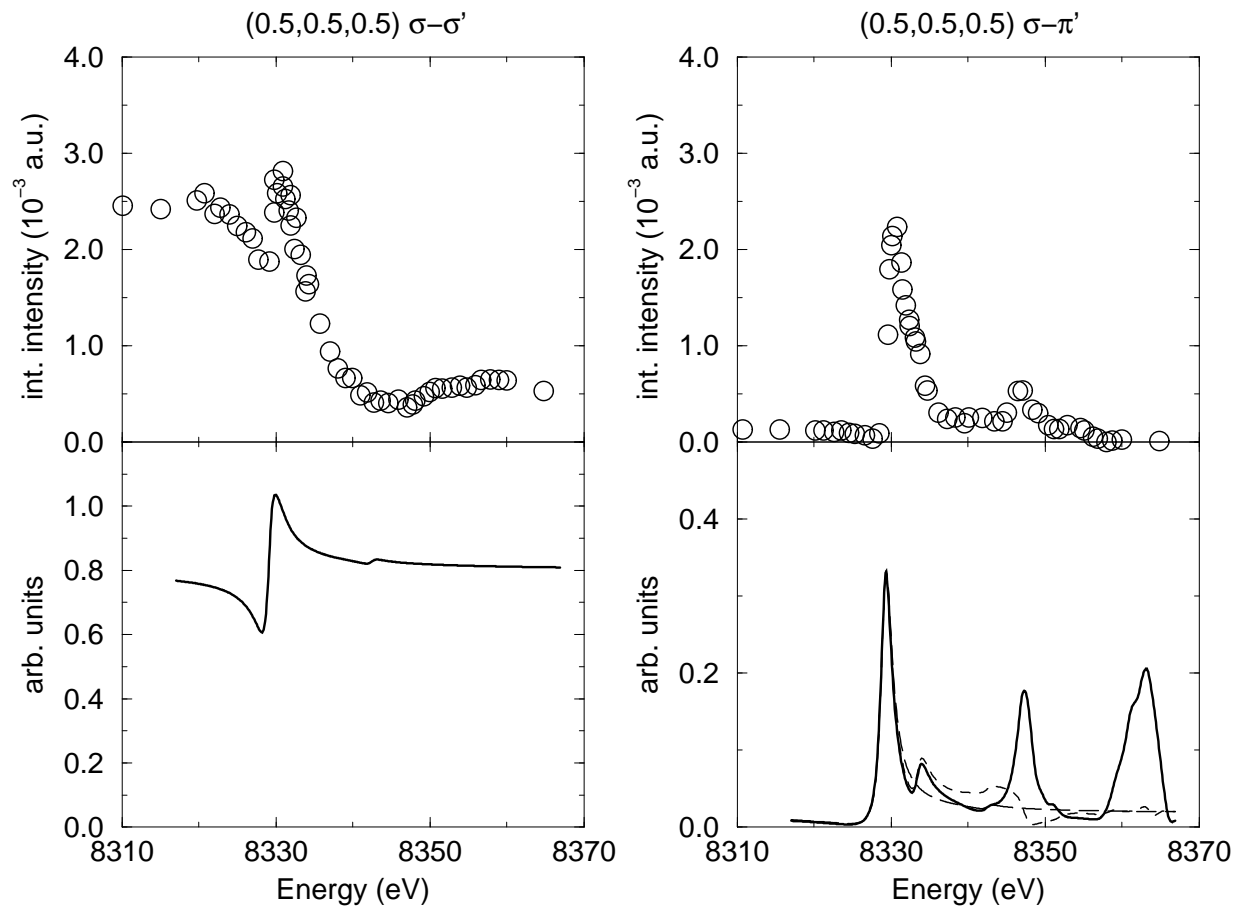


FIG. 4.

REVISED

J. Igarashi and M. Takahashi

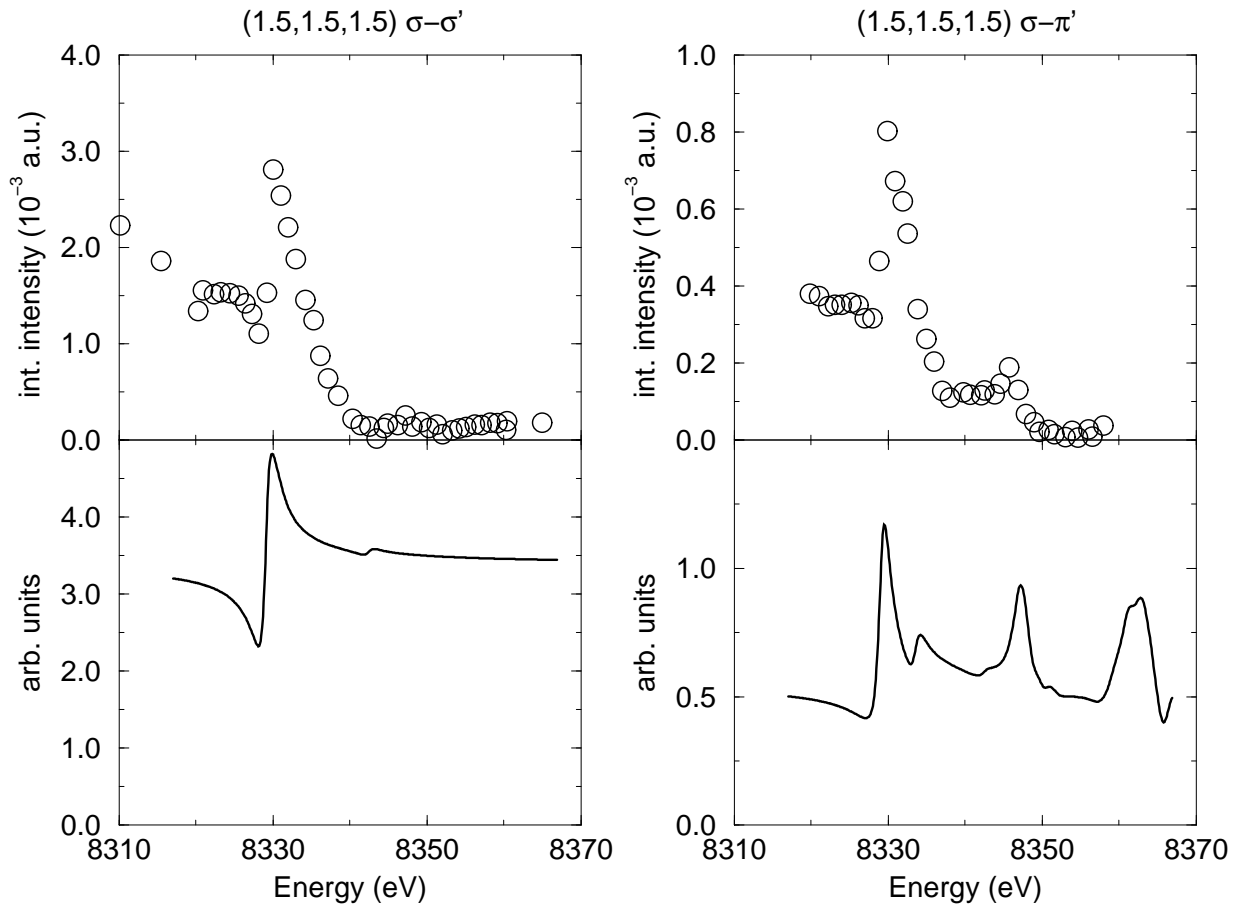


FIG. 5.

REVISED

J. Igarashi and M. Takahashi

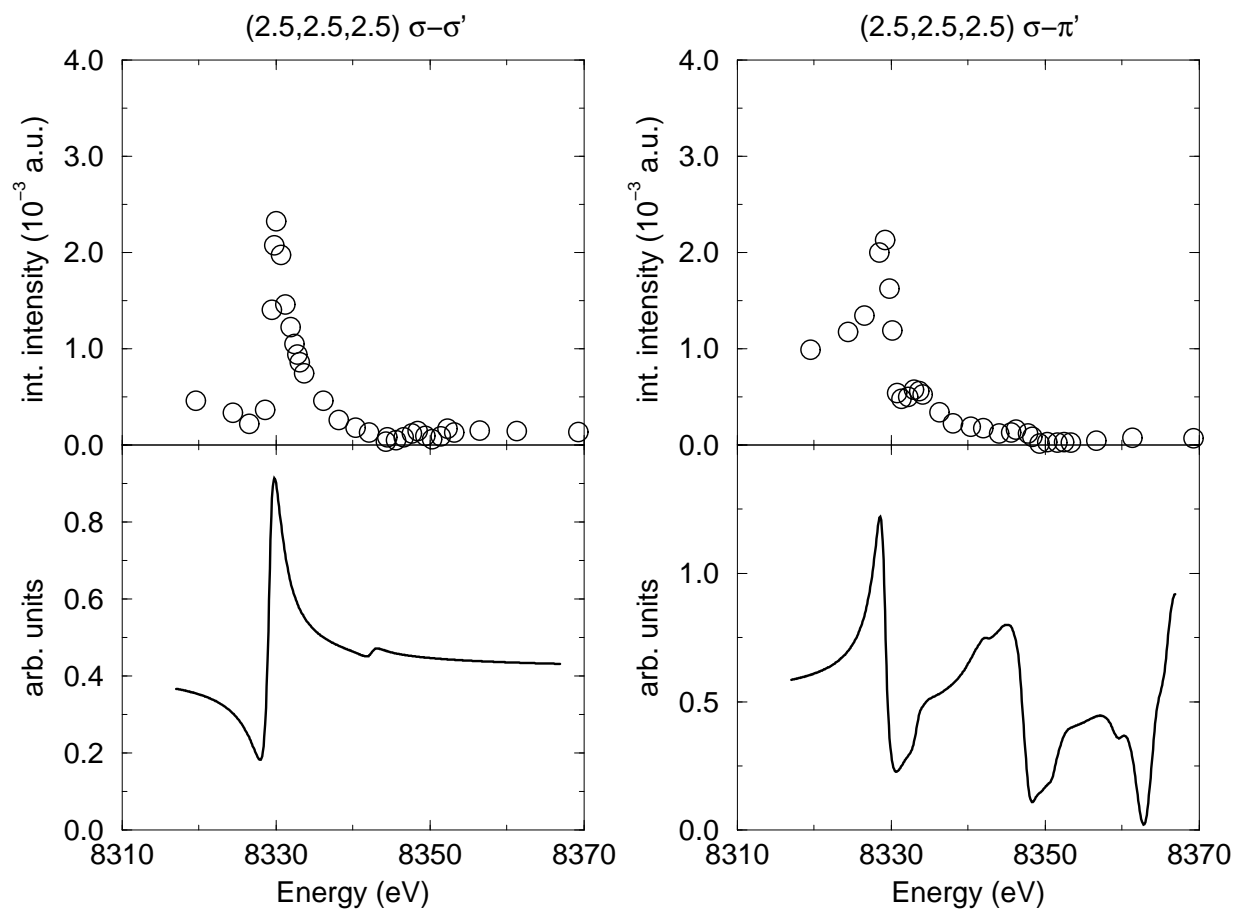


FIG. 6.

REVISED

J. Igarashi and M. Takahashi

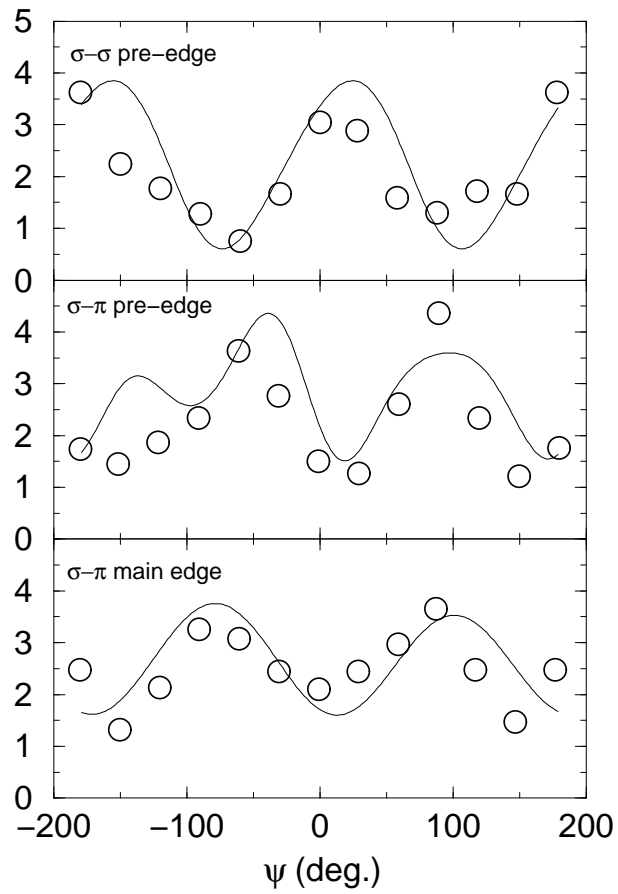


FIG. 7.

J. Igarashi and M. Takahashi